

Cross-sectional profile of photocarrier mobility in thin film solar cell via nongeminate recombination and charge extraction by linearly increasing voltage (cs-p-CELIV)

Noah B. Stocck, Miguel J. Young, Reg Bauld, Tianhao Ouyang, and Giovanni Fanchini*

*Department of Physics & Astronomy, The University of Western Ontario, 1151 Richmond St.
London ON, N6A 3K7, Canada*

Abstract - The ability to spatially resolve the carrier mobility profile along the cross section of micrometer-thin solar cells is vital both for fundamental studies in photovoltaics and as a quality control for reproducibly obtaining high conversion efficiencies in commercial solar cell modules. Presently, no technique capable of such an endeavor is available to the best of our knowledge. Here, we introduce a novel method capable of profiling the carrier mobility along the z -axis in thin-film photovoltaics. Our setup is based on the integration of photogenerated charge extraction by linearly increasing voltage (p-CELIV) with a scanning confocal optical microscope (SCOM) towards a cross-sectional sensitive p-CELIV (cs-p-CELIV) system. As geminate recombination of excess carriers is the most frequent radiative pathway for electrons and holes in solar cells at low power density of illumination, while nongeminate recombination dominates at high power, enhanced nongeminate recombination occurs at the SCOM focal plane. Thus, the cs-p-CELIV signal provides enhanced information on the mobility of all of the cross-sectional layers, except for the focal plane. By scanning the focal plane along the z -axis, the mobility profile can be derived. To demonstrate our technique, we use it to investigate the carrier mobility in a hydrogenated amorphous silicon (a-Si:H) solar cell. The mobility profile obtained by cs-p-CELIV correlates well with the H content profile, measured independently, and is in excellent agreement with models suggesting a critical role of Si-H bonding in locally determining the carrier mobility in a-Si:H.

* Corresponding author. E-mail: gfanchin@uwo.ca

1. Introduction

The design of advanced solar cells has led to tremendous efforts towards the development and characterization of high-quality semiconducting materials capable of converting sunlight into electrical power at low cost and high photoconversion efficiency.[1-3] A physical property of unique importance in solar energy materials and solar cells is the carrier mobility.[4,5] The mobility is a measure of the drift velocity at which charge carriers can diffuse in solids when acted on by an electric field.[6] The term carrier mobility refers in general to both electron and hole mobilities, which in semiconducting materials may be very different, and may also differ in the dark and upon illumination. The photoconversion efficiency of solar cells can be dramatically different depending on whether there are many carriers with low mobility or few carriers with high mobility in their active layer.[7] Almost always, higher mobility leads to better device performance,[8] all other device properties being equal. Development of laboratory techniques capable of measuring and imaging the carrier mobility in photo-active semiconducting layers is critical to improve the performance of thin-film solar cells incorporating these materials.

A well-established method for charge carrier mobility measurements relies on the Hall effect [9] in which a transversal voltage is created between two parallel faces of a sample at a constant magnetic field. A drawback of Hall effect mobility measurements is that these experiments require a very intense magnetic field in low-mobility photovoltaic devices, and they only carry information on the mobility of dark carriers. Differently from Hall effect experiments, mobility measurements in the time domain [10,11] are sensitive to the mobility of photoexcited carriers and do not require any magnetic field application. Time-domain photoexcitation techniques include time of flight (ToF) [10] and photo-conductivity recovery dynamics (PRD).[11] These techniques also have limitations, however. For example, PRD does not allow for mobility

measurements independent of the electrical transport properties, while ToF techniques offer reliable results only on relatively thick photoactive films, of a few μm or more.[12]

Photogenerated charge carrier extraction by linearly increasing voltage (p-CELIV) [13] is a time-domain mobility measurement technique that is applicable to devices with less restrictive thickness requirements than ToF.[12] Like ToF, p-CELIV is carried out by illuminating the sample with a nanosecond laser pulse to photoexcite a packet of charge carriers. Differently from ToF experiments, the voltage waveform used to induce a p-CELIV current transient is linearly increasing over time. A linear voltage ramp generates a significantly lower photocarrier drift velocity than a constant square waveform, as in ToF. Thus, at any device thickness and carrier mobility, the transient current maximum occurs at longer extraction times than ToF. This indicates that p-CELIV is capable of mobility measurements through thinner and less optically dense devices, typically down to 100 nm in hydrogenated amorphous silicon (a-Si:H) solar cells.[14]

A significant limitation of state-of-the-art time-domain photoexcitation techniques is that they are normally used only as one-data-point measurements, with no ability of profiling the mobility along the cross section of the active layer. While the suitability of p-CELIV to map the carrier mobility at micron-scale resolution along the x - y plane of organic photovoltaics has been reported,[15] demonstration of spatially resolved mobility scans along the z -axis requires optical resolution well below 1 μm , with the integration of p-CELIV with a scanning microscope, or *ad hoc* physical understanding of the carrier drift and recombination processes.

Here, we introduce a novel cross-sectional technique based on p-CELIV, which is capable of scanning the carrier mobility profile of a solar cell along the z -axis. To this end, a p-CELIV apparatus will be integrated with a scanning confocal optical microscope (SCOM) to induce strong light power density at the SCOM focal plane, but significantly lower illumination intensities above

and below. Nongeminate recombination can be defined as the recombination of a carrier (electron or hole) with an opposite carrier (hole or electron, respectively) that is not the same one with which it has been photogenerated. Thus, nongenerated recombination occurs only when high enough concentration of electron-hole pairs is locally generated due to high enough photon flux. Because of this, enhanced recombination of excess carriers in our system will occur at the focal plane due to nongeminate recombination processes [16,17] leading to diminished charge extraction from such a plane, and additional information on the device can be simultaneously acquired via confocal optical microscopy. This will allow for the returning of an array of p-CELIV signals by scanning one focal plane at a time, with each signal containing enhanced information on the mobility of all of the cross-sectional layers, with the exception of the focal plane, thus effectively implementing a cross-sectional p-CELIV (cs-p-CELIV) technique. Cross-sectional mobility profiles along the z -axis will thus be compiled through a specially developed algorithm that includes the discretization of the active layer in multiple slabs and considers nongeminate radiative recombination near the focal plane. Due to high sensitivity of p-CELIV at low thicknesses, demonstration of our mobility profiling technique for a 1.2 μm -thick solar cell is anticipated.

2. Experimental

2.1. Cs-p-CELIV apparatus

The p-CELIV and cs-p-CELIV measurements presented in this study are recorded using a Meshtel Intelite Q-switched laser at 527 nm wavelength, $t_p = 8$ ns pulse duration and 0.01-30 kHz repetition rate, as seen in Figure 1(a). The laser was connected to a WITec Alpha300 scanning confocal optical microscope [Figure 1(b)] by a step-index multimode optical fiber (Thorlabs Inc., 0.22 numerical aperture and 200 μm core diameter) which was wired to the SCOM pinhole. The

resulting beam had a $2.8 \cdot 10^{-5} \text{ cm}^2$ spot size at the focal plane, which allows for a high enough energy density (2.1 J cm^{-2} per pulse) to ensure strong non-geminate recombination in a-Si:H [16]. The SCOM is equipped with a computer-controlled piezo-scanner with 20-mm x - y travel range, 30-mm z -axis travel range, 0.1 nm z -axis resolution and $\pm 2\text{nm}$ repeatability, on which the sample was positioned, as shown in Figure 1(a). The SCOM is attached to a Hamamatsu H8259 photomultiplier operating in photon-counting mode. A cross-sectional SCOM micrograph in backscattering configuration is thus recorded at the same time as the cs-p-CELIV signal to establish a correlation between those data and the layered structure of the device.

In order to record cs-p-CELIV data at each (x, z) point of the device active layer, the end-of-pixel signal from the WITec Alpha 300 SCOM control unit is used to trigger the Q-switched laser. At a time lag $t_D = 200 \text{ ns}$, obtained through a tunable delay circuit, the triggering signal reaches a Stanford Research DS345 arbitrary function generator, which is set to produce a sequence of linearly increasing voltage ramps at $A = 2.45 \cdot 10^5 \text{ V s}^{-1}$ slope, $t_{\text{ramp}} = 40 \text{ }\mu\text{s}$ duration, $U_0 = -1 \text{ V}$ offset, and $100 \text{ }\mu\text{s}$ repetition rate. The function generator is connected to a bridge circuit on which a $1000\text{-}\Omega$ resistor is placed in parallel to the solar cell under investigation, as depicted in Figure 1(a). A Hantek 5200A digital scanning oscilloscope operated through a custom-made LabViewTM routine is connected to the photovoltaic device and is used to acquire the data. An ASCII file containing the cs-p-CELIV signal is recorded for each (x, z) pixel and stored in a personal computer for further analysis, as will be discussed in Sect. 3. A macroscopic p-CELIV measurement (i.e. without using the SCOM) was carried out as customarily reported in the literature [18-20] for comparison at $t_D = 200 \text{ ns}$, $A = 2.45 \cdot 10^5 \text{ V s}^{-1}$ slope, $t_{\text{ramp}} = 40 \text{ }\mu\text{s}$, $U_0 = -1 \text{ V}$, $100 \text{ }\mu\text{s}$ repetition rate, and $P = 1.9 \cdot 10^{-3} \text{ J cm}^{-2}$ per pulse energy density at the sample surface.

2.2. Solar cell used to validate this study

The solar cell used to validate our cross-sectional photo-CELIV measurement apparatus is a Sanyo AM-1411 hydrogenated amorphous silicon (a-Si:H) commercial thin-film module. In each module, three 29.6 x 11.8 mm devices are connected in series. For this study, a single device was detached from the module by cutting the glass substrate and has been electrically connected to the p-CELIV apparatus. The other two devices from the same module have been used for *post mortem* characterization, including scanning electron microscopy (SEM) and elastic recoil detection analysis (ERDA). This solar cell has been chosen because its specifications, which are representative of a large class of a-Si:H photovoltaics. As depicted in Figure 2(a) these devices have a *p-i-n* architecture [21] with an intrinsic a-Si:H region of about 1-2 μm thickness sandwiched between *p*-doped and *n*-doped regions that are significantly thinner, 30 nm or less.[21]

Post mortem cross-sectional analysis of a device from the same module was carried out on a Zeiss 1540 XB SEM, equipped with an energy dispersive X-ray (EDX) detector and a focused ion beam (FIB) apparatus. A trench was cut by Ga-ion FIB milling down to 4 μm , an in-depth penetration that was expected to be higher than the device thickness. The sample was subsequently tilted on the SEM stage, and a cross-sectional image [Figure 2(b)] was thus recorded. In this way, we were able to confirm that the active layer thickness is 1.2 ± 0.1 μm , with an 800 ± 100 nm thick aluminum top electrode, and an indium tin oxide (ITO) cathode of 1.0 ± 0.1 μm grown on a glass substrate. These figures are consistent with the typical design of a-Si:H *p-i-n* photovoltaics.[21] The assignment of each layer to Al, a-Si:H, ITO and glass was confirmed by EDX imaging, recorded for Al, Si, and Sn along the same cross section of the SEM image. Al and Si content maps are reported in Figures 2(c) and (d), respectively, and help to define the electrodes, active layer, and glass substrate, to unambiguously identify them by SCOM during cs-p-CELIV measurements.

The hydrogen profile in the a-Si:H solar-cell active layer was investigated using elastic recoil detection analysis (ERDA) and dynamic secondary ion mass spectrometry (SIMS) to establish a correlation between charge-carrier mobility and H content at each point along the cross section. ERDA was performed at Interface Science Western on a High Voltage Engineering Europa Tandetron ion accelerator, using a 1.7 MeV $^4\text{He}^+$ ion beam at 75° incidence angle with respect to the sample surface. Recoiled hydrogen was detected at a collection angle of 35° on a silicon diode retrofitted with a 700-channel analyzer and protected with a range foil to eliminate forward scattered ions from the incoming beamline. ERDA measurements were modelled using the SIMNRA simulation package.[22] In these simulations, the total thickness of the active layer was assumed to be 1,200 nm in accordance with SEM measurements, and the active layer was divided into 16 slabs at a constant thickness of 75 nm, for which different H contents were assumed.

SIMS was performed at Surface Science Western on a Cameca IMS-6f SIMS instrument. The sample was bombarded by a negatively polarized beam of oxygen particles (termed the primary ions) which sputtered its surface. The primary ions were subjected to an accelerating voltage of 10 keV, and raster scanned a $180\ \mu\text{m}$ -by- $180\ \mu\text{m}$ area. The sputtered material was ejected as a positively polarized secondary ion beam which was subject to a 4.5 keV accelerating voltage and analyzed in a magnetic sector mass spectrometer, which allowed for determination of the concentration of elements on the material's surface. Use of high-density primary ion beams allows for known sputtering rates, and therefore depth profiling is possible by measuring detected hydrogen as a function of time. This characterization was done in conjunction with ERDA measurements in order to give a second, independent measurement of the hydrogen profile. It also served as another, independent measurement of the thickness of the sample's a-Si:H active layer.

3. Model

3.1. Uniform active layer

In the models normally used for macroscopic, single-point, p-CELIV data analysis, [14,23] the active layer is assumed to be uniform along the device thickness, D . Under the additional assumptions of very different mobility for majority and minority carriers and low electrical conductivity of the active layer, the majority carrier mobility can be calculated from the signal transient as

$$\bar{\mu} = \frac{2D^2}{3At_m^2(1+0.36j_m/j_0)}, \quad (1)$$

where j_m is the maximum transient photocurrent, which occurs at a time t_m after the transient started, while j_0 is the constant current through the capacitive device due to a voltage ramp $V(t) = At$, with the voltage ramp starting at a time $t = 0$ and the laser pulsing at $t = -t_D$ (Figure 1a). The model assumes that, at any t , a region of the active layer at $0 < z < l(t)$ only contains minority photocarriers (majority photocarriers have already been extracted) while both majority and minority photocarriers are present at $l(t) < z < D$. Thus, the extraction layer $l(t)$ drifts across the device at a speed corresponding to the majority photocarrier drift velocity, $v_d(t) = \bar{\mu} E(t)$, where the electric field E linearly depends on t the same way $V(t)$ does, but is assumed to be z -independent. Then, both $v_d(t)$ and $\bar{\mu}$ in this model represent averages over the device z -axis.

Because equation (1) offers accurate mobility estimates only in devices that are relatively uniform along the z -axis cross section, a model for interpreting p-CELIV and cs-p-CELIV data in nonuniform devices is required in the present study. To derive such a model, we will first divide the device's active layer into N slabs of identical thickness, D/N , with $N \gg 1$, as seen in Figure 3(a). At a time $t = t_k$ ($k = 1, \dots, N$) after the transient, majority photocarriers are only present in,

and extracted from, slabs at $i > k$, where τ_k is the time required for carriers to diffuse through the k -th slab, which is equal to the time taken by the extraction layer to drift across the slab. At $t = t_k$, the drift velocity, averaged between slabs $i = 1, \dots, k$, takes the form

$$\bar{v}_{0,k}(t) = \frac{l(t)}{t} = \bar{\mu}_{0,k} E(t) = \frac{kD}{Nt_k} = \frac{\mu_1 + \dots + \mu_k}{k} \frac{A}{D} t_k, \quad (2)$$

where μ_i is the majority photocarrier mobility in the i -th slab while $\bar{\mu}_{0,k}$ is averaged over the first k slabs. In a nonuniform device, the phase velocity of the extraction layer, offered by equation (2), is different from the instantaneous group velocity across k , which is given by

$$v_k(t) = \frac{dl(t)}{dt} = \mu_k E(t) = \frac{D}{N\tau_k} = \mu_k \frac{At_k}{D}. \quad (3)$$

By explicitating t_k from the last two terms in equation (2) and replacing it into equation (3), an expression for τ_k , the time required to diffuse through the k -th slab can be derived:

$$\tau_k = \frac{D}{k\mu_k} \sqrt{\frac{\mu_1 + \dots + \mu_k}{NA}}. \quad (4)$$

While τ_k may contain useful information on μ_k , it largely depends on $\bar{\mu}_{0,k}$, averaged over k slabs. A measurable quantity more meaningfully related to the local properties at k is then required for cross-sectional p-CELIV measurement interpretation. The total photocurrent extracted at $t = t_k$ during the transient, is the sum over all of the infinitesimal contributions from the carrier-containing slabs at $i > k$. This sum can be expressed either by an integral or a discrete summation over the slabs, as

$$j_{k,N} = \int_{l(t)}^D n(z) e \mu(z) E(z, t_k) \frac{dz}{D} = e (n_{k+1} \mu_{k+1} + \dots + n_N \mu_N) \frac{At_k}{D} = e \sqrt{\frac{A}{N}} \frac{(n_{k+1} \mu_{k+1} + \dots + n_N \mu_N)}{\sqrt{\mu_1 + \dots + \mu_k}} k, \quad (5)$$

where $n(z)$ and n_k are the majority photocarrier densities in the continuous and discrete picture, respectively, and e is the elementary charge.

The approach normally used for extracting the carrier mobility is to determine the

maximum conditions, t_m and j_m . [23] With this approach, the maximum of the photocurrent transient, derived by differentiating $j_{k,N}$ over time in equation (5), is normalized by the constant dark current through the capacitive device leading, for example, to equation (1). By differentiating equation (5), the slope of the current transient at a generic time t_k takes the form

$$\Delta_k \equiv \frac{j_{k,N} - j_{k-1,N}}{\tau_k} = \frac{eA}{D} \left[\frac{(n_k \mu_k + \dots + n_N \mu_N)k}{\sqrt{\mu_1 + \dots + \mu_k}} - \frac{(n_{k-1} \mu_{k-1} + \dots + n_N \mu_N)(k-1)}{\sqrt{\mu_1 + \dots + \mu_{k-1}}} \right] \frac{k \mu_k}{\sqrt{\mu_1 + \dots + \mu_k}}. \quad (6)$$

By assuming $\mu_1 + \dots + \mu_{k-1} \approx \mu_1 + \dots + \mu_k$ at denominator, $n_k = \text{const.}$, and imposing $\Delta_k = 0$, it can be verified that $j_{k,N}$ reaches a maximum at

$$m \approx (\mu_m + \dots + \mu_N) / \mu_m, \quad (7)$$

which can be replaced into equation (6) leading to an expression for $\bar{\mu}$ equivalent to equation (1) if $\mu_1 = \dots = \mu_N = \bar{\mu}$. Because the extraction current is $j_{0,N} = 0$ at the onset of the linearly increasing voltage, setting $k = 1$ in equation (6) simplifies it into

$$n_1 \mu_1 + \dots + n_N \mu_N = \frac{D}{eA} \Delta_1. \quad (8)$$

Equation (8) can then be used as an alternative to equation (1) to interpret the macroscopic, single-point, p-CELIV data in which both $n_k \approx \bar{n}$ and $\mu_k \approx \bar{\mu}$ are assumed to be constant and independent of i . From our cs-p-CELIV measurements, we have a set of N different values of $\Delta_1(z_o)$, obtained at varying microscope focal planes (z_o) scanned from $k = 1$ to N . Therefore, a system of N equations of the form (8) in N unknowns can be used to relax the uniform-mobility assumption, and obtain a set of values of μ_i along the z -axis, under specific assumptions for n_k that, in general, is also not constant. We will now focus on the case in which the variations of $n_k = n(z_k)$ are locally controlled by nongeminate recombination [16] due to locally stronger photon flux at the focal plane.

3.2. Nonuniform active layer and nongeminate recombination

The model for interpreting cs-p-CELIV data in a nonuniform solar cell active layer is presented in Figure 3(b). Because the active layer is relatively thin over Δz , the focal depth of our optical microscope, the absorbed photon flux, corresponding to the flux of electron-hole pairs photogenerated at any slab, is modelled to have a Gaussian profile centered at the focal plane z_f :

$$\beta(z - z_f) = (\sigma/\Delta z) e^{-\left(\frac{z-z_f}{\Delta z}\right)^2}, \quad (9)$$

where σ is determined by the laser beam intensity and the sample's optical absorption coefficient at the laser wavelength. With a known optical absorption coefficient, α , σ can be chosen to account for the beam attenuation in the sample. The absorbed photon flux β (in photons $\text{cm}^{-2} \text{s}^{-1}$) determines the distance between photo-generated electrons and holes ($e-h$) at the depth z , which is proportional to $t_p\beta$. [24]

Street [16] showed that β determines the amount of non-geminate recombination through the randomized distance between $e-h$ pairs, which is therefore controlled by σ and Δz . As shown in Figure 3(c) geminate recombination dominates where the distance between photo-generated $e-h$ pairs is high. In such case, the density of $e-h$ pairs available for dissociation and extraction is linear in the photon flux, and proportional to the laser power. When $t_p\beta$ becomes comparable to the distance between the electron and hole in an $e-h$ pair, nongeminate recombination becomes significant, with $n < \min(\bar{n})$ due to the diminished radiative recombination time which may become comparable to τ_k , the transit time. Thus, the concentration of extracted charges is locally diminished at $z \in z_f \pm \Delta z$, with an exponentially decaying trend due the exponential decay of the carrier concentration at a shorter radiative recombination time:

$$n(z - z_f) = \bar{n}(z) e^{-\beta(z-z_f)/\beta_0}, \quad (10)$$

where β_0 is a constant expressing the probability of nongeminate recombination. Equation (10)

can be replaced into equation (8) to determine $n_k = n(z_k)$ at each slab z_k , thus effectively implementing a mobility-mapping SCOM in which confocal optical detection is replaced by selective z -axis detection due to locally high nongeminate recombination in the proximity of the focal plane z_f , which is scanned over the device thickness. In other words, as nongeminate recombination dominates at higher power, it predominantly occurs about the SCOM focal plane, and cs-p-CELIV measurements provide enhanced information on the mobility from all of the cross-sectional layers, except for the proximity of the focal plane.

In order to demonstrate the major aspects of our model, let us assume, for the sake of simplicity, a case of high cross-sectional resolution (with $\Delta z \ll D/N$) and very strong illumination. In such case, $n_k \approx 0$ for $k=f$ and $n_k \approx \bar{n}_k$ elsewhere, as seen in Figure 3(b). \bar{n}_k can thus be determined [13] from a macroscopic, single point, p-CELIV measurement and by considering attenuation of the beam due to absorption as

$$\bar{n}(z) = \frac{3\varepsilon}{2e\bar{\mu}} \frac{j}{j_0 t_m} e^{-\alpha \cdot \Delta z \cdot k}, \quad (11)$$

where ε is the dielectric constant of the active layer, α is the optical absorption coefficient, and the other quantities are the same as in equation (1). A system of N equations in N unknowns can be written from equation (8) as

$$[\mathbf{1} - \mathbf{I}] \begin{bmatrix} \mu_1 \\ \dots \\ \mu_N \end{bmatrix} = \frac{2D}{3A\varepsilon} \frac{\bar{\mu} j_0 t_m}{j_0} \begin{bmatrix} e^{\alpha \cdot \Delta z} \Delta_1(z_f = z_1) \\ \dots \\ e^{\alpha \cdot \Delta z \cdot N} \Delta_1(z_f = z_N) \end{bmatrix}, \quad (12)$$

where $\mathbf{1}$ is an N -by- N matrix of ones and \mathbf{I} is the identity matrix. This system can thus be solved for μ_1, \dots, μ_N by inverting $[\mathbf{1} - \mathbf{I}]$, and provides a first-order analytical framework to extract mobility profiles from $\Delta_1(z_f)$ measured by cs-p-CELIV at varying SCOM focal planes, along with a macroscopic single-point p-CELIV measurement of the same system. If n_k is not negligible for $z_k = z_f$ but $n_k(z_k = z_f) < \overline{n(z_k \neq z_f)}$, or Δz is not small over D/N , then a numerical model more

sophisticated than equation (12) will be required, and such model will have to treat σ and β_0 as adjustable parameters, as discussed in section 4.

4. Results and Discussion

Figure 4 shows the data collected in a typical cs-p-CELIV experiment at varying focal plane on an a-Si:H solar cell. In Figure 4(a), a cs-p-CELIV current transient at a specific focal plane ($z_f = z_1$, at the interface with the ITO cathode) is presented as an example. From a set of experimental current transients at $z_f = z_1, \dots, z_N$, the maximum photocurrents $j_m(z_f)$ and times $t_m(z_f)$ are determined through an automated MatlabTM routine. Figures 4(b) and (c) show examples of cross-sectional maps of $j_m(z_f)$ and $t_m(z_f)$ respectively, where, in addition to the z -axis, the x -axis parallel to the solar cell surface was also scanned for 12 μm to ensure lateral uniformity. From panel (c) it can be noticed that t_m does not have any appreciable dependence on z_f . Conversely, panel (b) shows a significant decrease of $j_m(z_f)$ when z_f lies within the a-Si:H solar cell active layer. Specifically, the decrease in j_m is 20% at about one third of its cross-sectional depth. This leads us to suspect high sensitivity of j_m to local radiative recombination events triggered by higher photon flux deposited at $z = z_f$, for example nongeminate recombination as for equation (12).

From $j_m(x, z_f)$ and $t_m(x, z_f)$ in Figures 4(b-c), the corresponding map of $\Delta_1(x, z_f) \approx j_m/t_m$ can be generated and is shown in Figure 4(d). $\Delta_1(x, z_f)$ can be plugged into equation (12) to derive the cross-sectional mobility profile. Additional parameters required by equation (12) were derived from a macroscopic, single point, p-CELIV experiment, carried out after removing the microscope objective, which enables very high focal depth due to the coherence of the laser beam. From these measurements, an average mobility $\bar{\mu} = 6 \text{ cm}^2 \text{ V}^{-1} \text{ s}^{-1}$, consistent with previous reports for a-Si:H, [25] was estimated from $t_m = 6.5 \text{ }\mu\text{s}$ and $j_m/j_0 = 0.0624$, which were used in equation (1). $D = 1.2$

μm , obtained from Figure 2(b), and the voltage ramp ($A = 2.45 \cdot 10^5 \text{ V s}^{-1}$) applied to the function generator were also used. Because the a-Si:H solar cell was shown to be very uniform along the x -axis, data points along x were averaged to improve the signal-to-noise ratio, as shown in Figure 5(a), which reports (red dots) the values of $\Delta_1(z_f)$ actually used to determine the mobility profile along the z -axis from equation (12).

Figure 5(b) presents the cross-sectional mobility profile along z , derived from $\Delta_1(z_f)$. $\mu(z)$ clearly shows a nonuniform and triangular profile, with the majority carrier mobility gradually increasing from the Al anode up to three quarters of the active layer thickness, with a subsequent and sudden decrease in the proximity of ITO, possibly at the onset of the p -type doped a-Si:H interface with the cathode [see Figure 2(a)]. Self-consistency of the model used to derive the mobility profile can be tested by plugging $\mu_f = \mu(z_f)$ into equation (6) and extracting a calculated value of $\Delta_1(z_f)_{Calc}$, which must favourably compare with its experimentally measured counterpart, $\Delta_1(z_f)_{Meas}$. To this end, a hypothesis on n_k to be used in equation (6) is necessary. If we assume equation (10) along with a Gaussian beam profile as in equation (9), a very accurate estimate of $\Delta_1(z_f)_{Calc}$ can be obtained with $\sigma = 6 \cdot 10^7 \text{ cm}^{-1} \text{ s}^{-1}$ and $\beta_0 = 1.0 \text{ cm}^{-2} \text{ s}^{-1}$, as shown in Figure 5(a). This calculation of $\Delta_1(z_f)_{Calc}$ can be performed assuming \bar{n} independent of z or decaying exponentially with z due to absorption, both of which are shown in Figure 5(a), and the results are similar, suggesting that the effect due to absorption is minimal over the thickness of our sample at this wavelength. Even though our calculation converges in one iteration with a standard deviation $\Sigma |\Delta_1(z_f)_{Calc} - \Delta_1(z_f)_{Meas}| / \Delta_1(z_f)_{Calc}$ better than 2% for both carrier density profiles, this can easily be extended to a multi-iteration routine by recalculating the mobility profile until a minimum threshold is reached. Although Figure 5(a) shows that this iterative approach is not necessary for the reported a-Si:H device, it may become essential for analyzing other solar cells with more

varying mobility profiles. This option increases the flexibility of our mobility profile characterization tool.

A possible explanation for the triangular mobility profile across the investigated device is related to the cross-sectional variation of the hydrogen content in the a-Si:H active layer. Hydrogen is known to locally effect the mobility of a-Si:H because of its ability to passivate the coordination defects in this amorphous system.[26] While atoms in crystalline Si are all four-fold coordinated, a relatively large number (up to 10^{20} cm^{-3} [16]) of Si sites in a-Si are three-fold coordinated, which results into dangling bond states situated at mid-gap, as shown in Figure 6(a). These gap states act as traps for photogenerated electrons and holes and limit their mobility. Introduction of hydrogen during a-Si:H growth leads to the replacement of a significant proportion of dangling bonds by relatively strong SiH_n groups with bonding and antibonding states sitting in the valence and conduction bands, respectively, and thus some defects become passivated [27]. Figure 6(b) demonstrates the role of dangling bond passivation in removing electronic states from mid-gap in a-Si:H, which may be expected to locally provide beneficial effects to the carrier mobility as mid-gap states may act as charge traps.[27] Thus, fewer charge traps and higher mobility are expected in slabs where the H content is locally higher.[28]

The result of ERDA measurements and simulations performed on the active layer of our a-Si:H solar cell is displayed in Figure 7(a) and confirms the predictions drawn from H content profiling. This figure also shows the ERDA signal calculated from the SIMNRA code [22] assuming elastic He-H collisions. It can be observed that a uniform H profile does not satisfactorily simulate the ERDA signal, while the nonuniform profile in Figure 7(b) perfectly fits the experimental data. Figure 7(b) also shows the hydrogen profile obtained from SIMS measurements, which further confirms this nonuniform distribution. Comparison of Figure 7(b)

and 5(b) indicates that, at least qualitatively, a correlation between H content and carrier mobility can be drawn.

Figure 7(c) shows the hydrogen content from both experiments as a function of the mobility. Red and black circles show the data on the top half of the active layer, while squares show the data in the bottom half. While the SIMS and ERDA data don't match exactly, they show the same general trend of mobility increasing with hydrogen content for the top half of the device, and no dependence on hydrogen on mobility in the bottom half. In the proximity of the Al anode, the electron mobility is expected to be the most affected by positively charged traps, which explains the direct correlation between H concentration and improved mobility, consistent with H passivation of electron-trapping gap states, as previously shown in Figure 6. In the proximity of the ITO cathode, the H content plays a less significant role, and our measured mobility is independent of H content, as p-CELIV is overwhelmingly sensitive to majority carriers that in our a-Si:H device are known to be electrons.

The picture that can be drawn from our cs-p-CELIV measurements is in excellent agreement with the commonly accepted doping mechanism of a-Si:H,[16, 29] which is profoundly different from part-per-million substitutional doping well established in its crystalline counterpart (c-Si).[30] In amorphous a-Si:H, phosphorous and boron impurities act as dopants with a physical mechanism that is significantly different from c-Si. In a-Si:H, P and B need to be incorporated at part-per-cent levels [31] to provide a suitable amount of minority and majority carriers. In a-Si:H, virtually all of the group 13 and group 15 impurities are, in fact, trivalent and pentavalent and the role of acceptors and donors is actually played by the residual amount (10^{17} cm^{-3} , or less [16]) of dangling bonds not passivated by hydrogen, with the role of impurities being limited to charging a suitable amount of dangling bond states.[16] Due to their excellent correlation with cross-

sectional H content, our cross-sectional majority-carrier mobility measurement, are in excellent agreement with the physical understanding of the device used to validate them.

While cross-sectional mobility profile correlates well with the hydrogen profile detected by ERDA, it is worth noting that H profiling in a-Si:H requires sophisticated ion measurements. Conversely, our cs-p-CELIV benchtop system is suitable to work in air and is simple to implement at low budget costs. Furthermore, cs-p-CELIV is a non-destructive technique and, differently from vacuum-related characterization methods, it is suitable to rapid quality control in large commercial panels made of thin-film solar cells. This is also witnessed by the possibility to perform line scans along the x -axis, as shown in Figure 4.

5. Conclusion

In conclusion, the integration of p-CELIV measurements with a SCOM has allowed for spatially dependent measurements of the charge carrier mobility along the z -axis of a micrometer-thick solar cell, by exploiting enhanced non-geminate recombination at the SCOM focal plane. The mobility profile that was obtained correlates well with the hydrogen profile of the a-Si:H active layer, and adds insight into the role of hydrogen in the optoelectronic properties of a-Si:H. While our technique was demonstrated on an a-Si:H device, it is widely applicable to a wide range of thin-film photovoltaic devices.[32] The dominance of non-geminate recombination at high illumination is a general property of a vastity of solar cell materials, and therefore we are not restricted by sample. As we have proven, the technique we developed allows for unprecedented cross-sectional investigations into the devices' structure. In summary, cs-p-CELIV is a powerful non-destructive technique and, differently from vacuum-related characterization methods, it is suitable to rapid quality controls in large commercial panels made of thin-film solar cells, in which reproducible and carefully engineered mobility profiles across the active layer are vital.

Acknowledgements

We would like to thank Dr. Todd Simpson and Mr. Tim Goldhawk of Western University's Nanofabrication Facility for technical support with FIB, SEM and EDX analysis. We would also like to thank Dr. Lyudmila Goncharova and Mr. Jack Hendriks of Interface Science Western for their assistance during the ERDA measurements. This study was supported by the Canada Research Chair secretariat, the Canada Foundation for Innovation, and the Natural Sciences and Engineering Research Council of Canada (NSERC) under the Discovery Grant program.

Figure Captions

Figure 1- (a) Schematic of p-CELIV experiment, in which laser pulse is incident on solar cell and linearly increasing waveform is applied; the resulting photo current transient measured on a digital scanning oscilloscope. Maximum extraction current occurs at t_m . (b) Diagram of p-CELIV combined with SCOM to form a cs-p-CELIV setup, where a 527-nm laser beam is pulsed through the pinhole, and then focused onto the focal plane z_f , which is varied by using the piezo-scanner on which the solar cell is positioned.

Figure 2- Thin-film a-Si:H based *p-i-n* solar cell used as test sample in this work, as well as the need for their cross-sectional investigation. (a) diagram of device architecture compared to (b) cross-sectional SEM images. (c) Cross-sectional EDX imaging in the same area as in panel b for Al and (d) Si composition to identify the electrodes and a-Si:H active layer for enhanced interpretation of subsequent cs-p-CELIV investigations.

Figure 3- (a) P-CELIV model for uniform active layer, based on a multi-slab discretization of the device. Selected physical quantities appearing in equations (1)-(8) are indicated. (b) Cs-p-CELIV model as in (a) with increased carrier generation at the focal layer (green) due to nongeminate recombination. The type of enhanced recombination shown here allows for cross-sectional study of the device. (c) The origin of i) geminate and ii) nongeminate recombination from higher concentration of radiatively recombining excess carriers at the focal plane is presented. Nongeminate recombination can be defined as the recombination of a carrier (electron or hole) with an opposite carrier that is not the same one with which it has been photogenerated.

Figure 4- (a) Typical p-CELIV current transient with SCOM confocal plane set at a specific slab ($z_f = z_1$, in this case) of the a-Si:H solar cell active layer. (b) Photocurrent maximum (j_m) as a function of x and z_f . The minimum of j_m at $z_f \approx 2 \mu\text{m}$ is situated at about three-quarters of the a-

Si:H layer thickness. (c) Maximum transient time, t_m as a function of x and z_f . Differently from j_m , the value of t_m has little dependence on z_f . (d) Photocurrent transient ramp $\Delta_1(x, z_f)$ that also presents a minimum at about three-quarters of the a-Si:H layer thickness, due to the minimum of $j_m(z_f)$. $\Delta_1(x, z_f)$ is then averaged along x , and used to determine the mobility at each z -axis slab.

Figure 5- (a) Measured $\Delta_1(z_f)$ corresponding to $\Delta_1(x, z_f)$ averaged over each x -line. per focal plane (dots) and calculated $\Delta_1(z_f)$ (solid lines with and without attenuation of light due to absorption considered) from equations (9)-(10) and (5). It can be observed that the calculated values match the measured one indicating that the mobility values are accurate, with a less than 2% standard deviation. (b) Mobility profile determined from equation (12) showing a triangular profile. The dashed line is a visual aid.

Figure 6- (a) Random a-Si:H network, with dangling bonds represented by dots. (b) Dangling bond states lead to charge traps at mid-gap, which significantly affect the carrier mobility. A schematic of the a-Si:H density-of-states of is shown by solid lines, while dashed lines in the gap are represent traps states that are eliminated via H passivation of dangling bonds.

Figure 7- (a) ERDA hydrogen profile and comparison with SIMNRA simulation with simulated data used to determine the H atomic percentage. It can be noticed that a uniform H profile is not able to account for the measured ERDA spectrum at the lowest channel energies. (b) H profile along the a-Si:H active layer, showing significant variations as obtained from ERDA (bars) and SIMS. (c) Correlation between H content and carrier mobility, showing an increasing majority (n -type) carrier mobility at increasing H content due to dangling bond passivation for the bottom 50% of the z -axis profile. This is consistent with data obtained from both ERDA and SIMS. Majority (n -type) carrier mobility is not dependent on the H content in the top 50% of the z -axis, where a closer correlation between minority (p -type) mobility and H content would be expected.

Figure 1

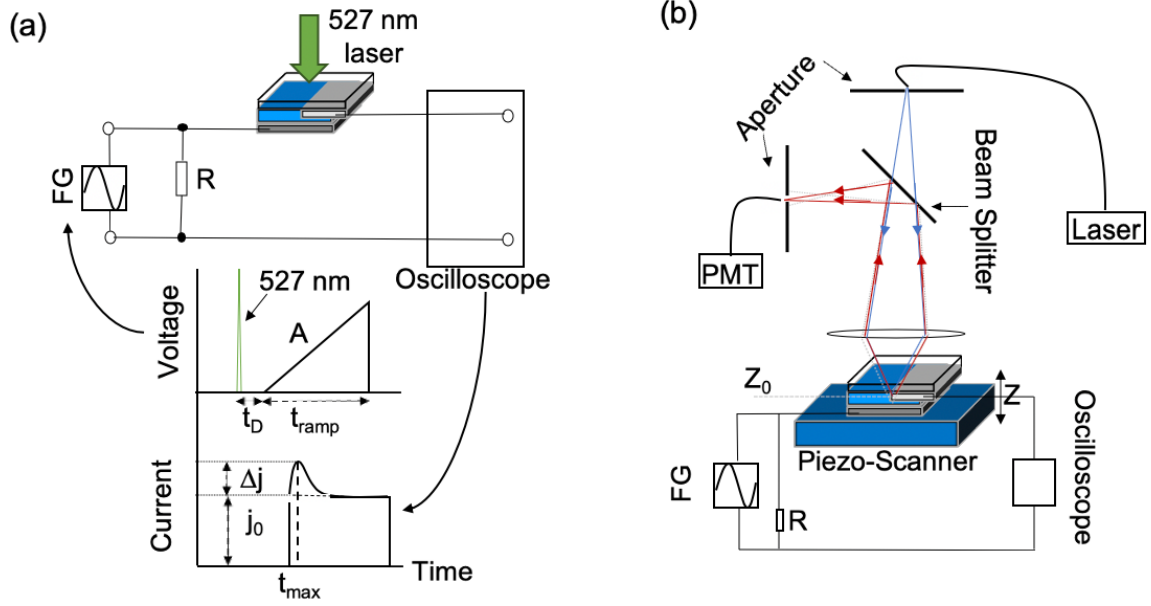


Figure 2

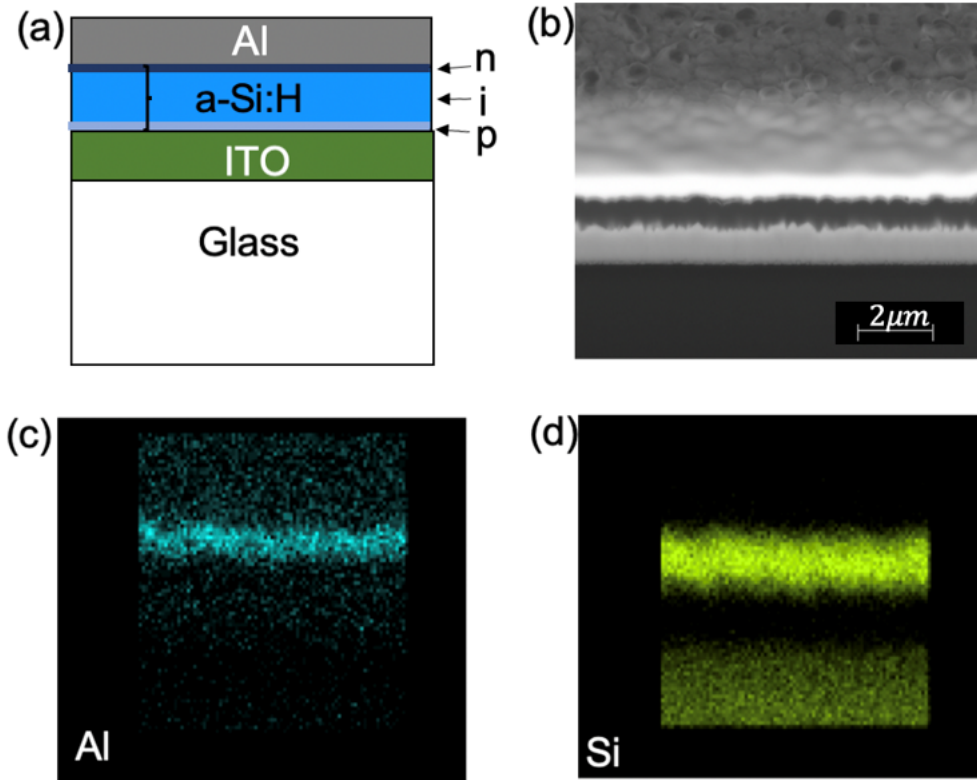


Figure 3

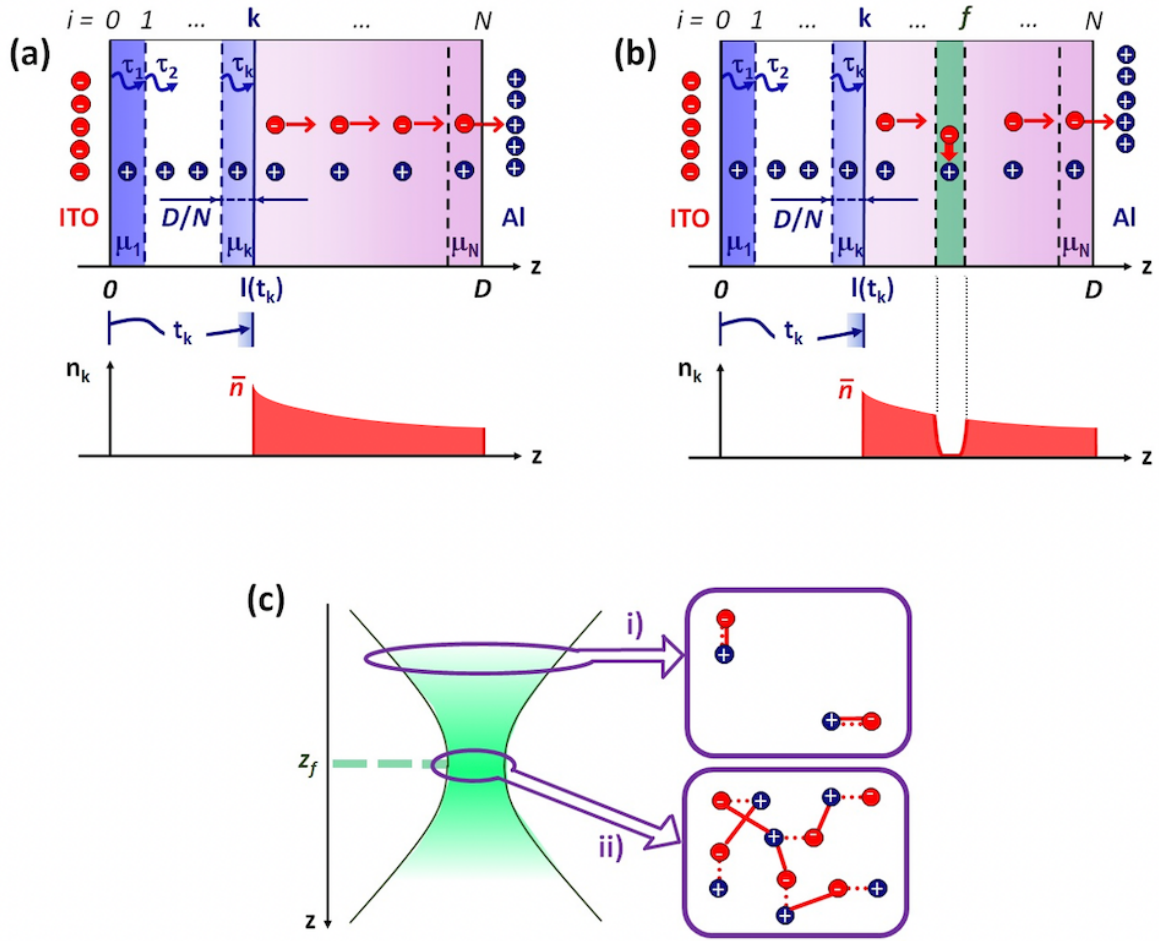


Figure 4

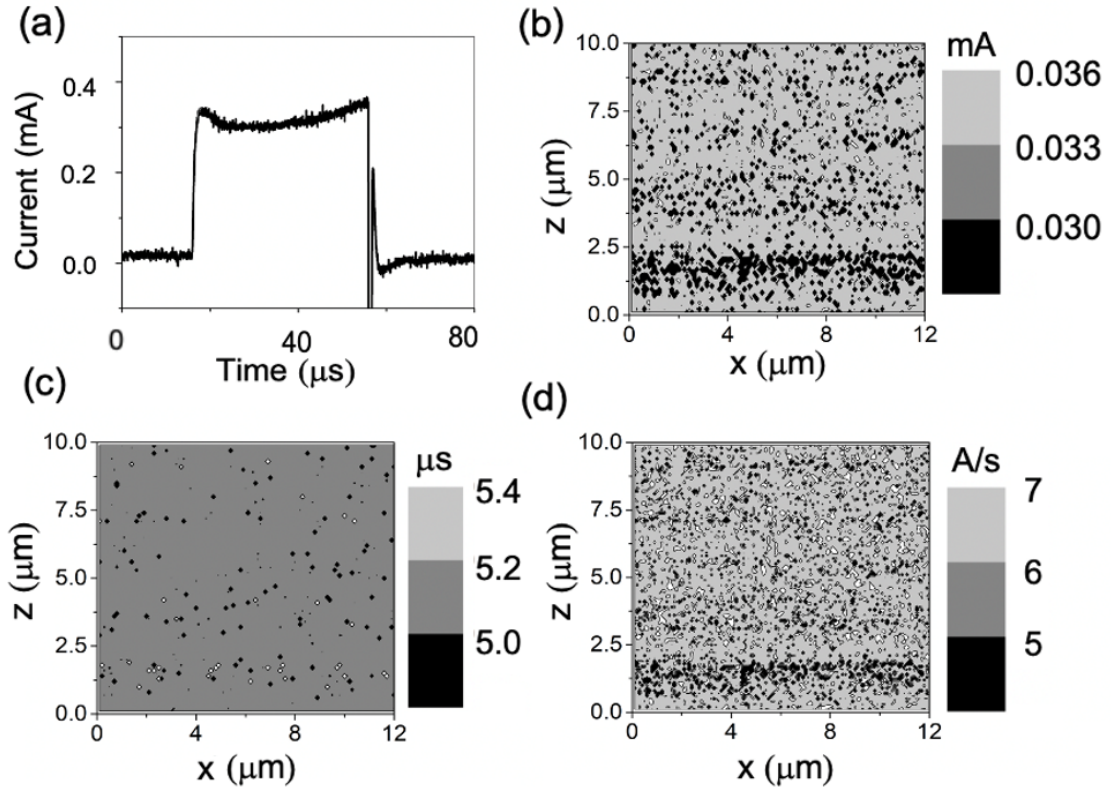


Figure 5

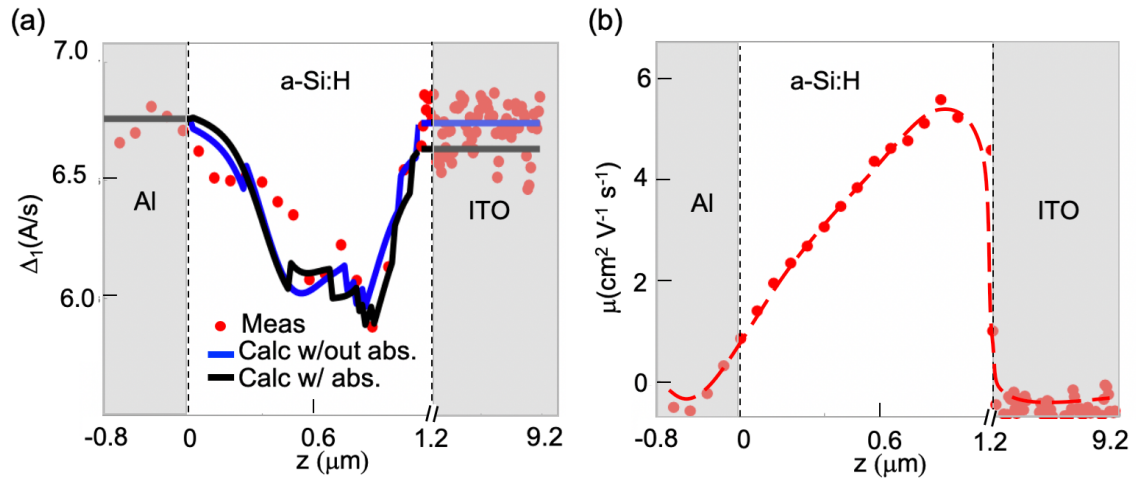


Figure 6

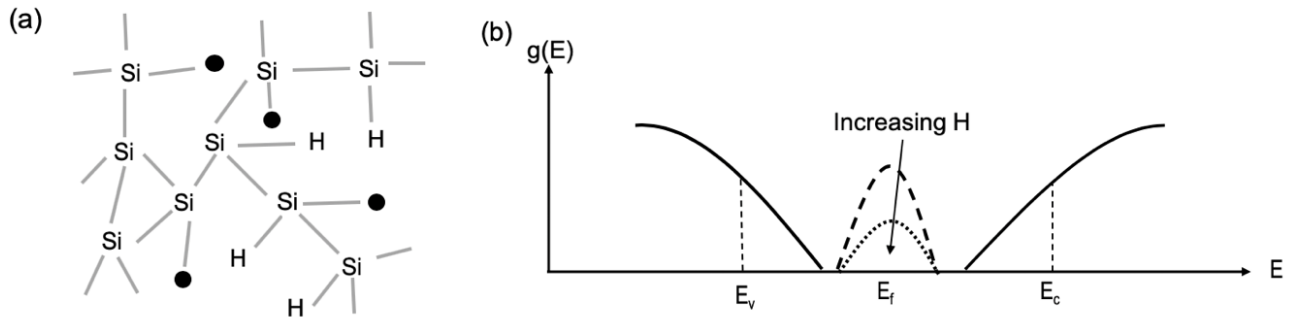
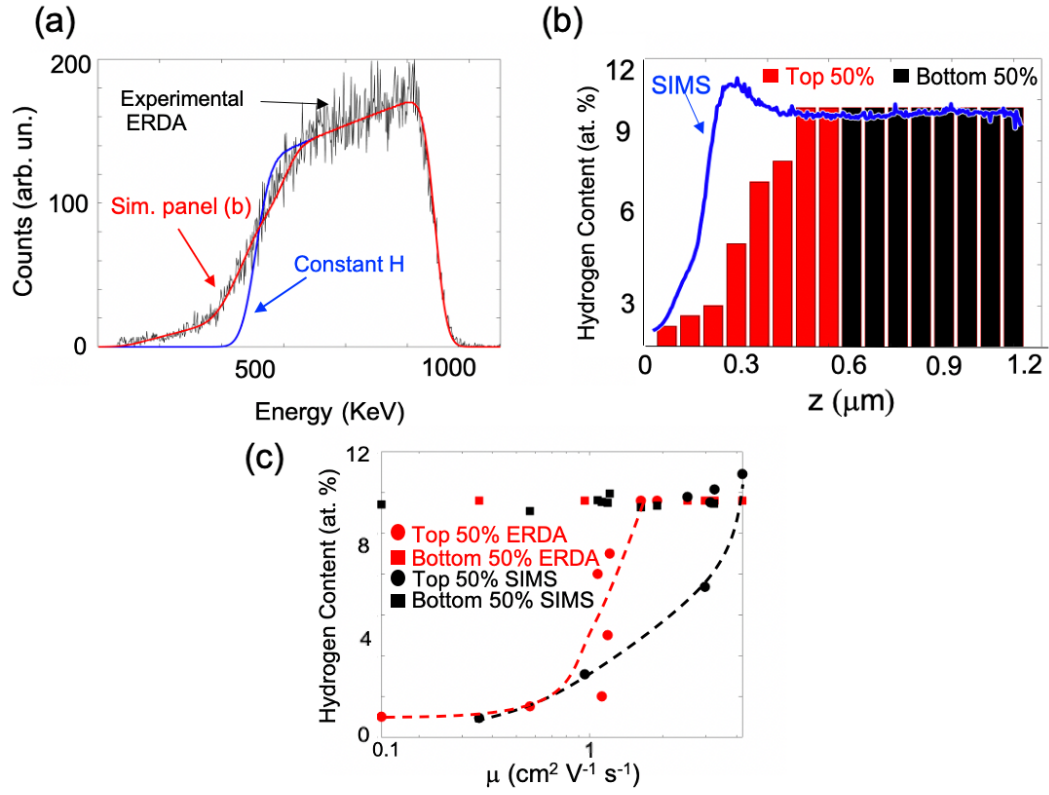


Figure 7



References

1. A.V. Shah, R. Platz, H. Keppner
Thin-film silicon solar cells: A review and selected trends
Solar Energy Materials and Solar Cells 38, 501-520(1995)
2. P. Roy, N. K. Sinha, S. Tiwari, A. Khare
A review on perovskite solar cells: Evolution of architecture, fabrication techniques, commercialization issues and status
Solar Energy 198 (2020) 665-688
3. M. Green
Thin-film solar cells: review of materials, technologies and commercial status
Journal of Materials Science: Materials in Electronics 18, 15-19(2007)
4. W. Tress, K. Leo, M. Riede
Optimum mobility, contact properties, and open-circuit voltage of organic solar cells: A drift-diffusion simulation study
Phys. Rev. B 85, 155201(2012)
5. A. Privkas, N. Sariciftci, G. Juška, R. Österbacka
A Review of Charge Transport and Recombination in Polymer/Fullerene Organic Solar Cells
Prog. Photovolt: Res. Appl. 15, 677-696(2007)
6. E.A. Schiff
Low-mobility solar cells: a device physics primer with application to amorphous silicon
Solar Energy Materials and Solar Cells 78, 567-595(2003)
7. G. Chen, Y. Chen, C. Lee, H. Lee
Performance improvement of perovskite solar cells using electron and hole transport layers
Solar Energy 174, 897-900(2018)
8. J. Shieh, C. Liu, J. Meng, S. Tseng, Y. Chao, S. Horng
The effect of carrier mobility in organic solar cells
J. Appl. Phys. 107, 084503(2010)
9. P. LeComber, W. Spear, D. Allan
Transport studies in doped amorphous Silicon
J. Non-Cryst. 32, 1-15(1979)
10. W. Spear
The Hole Mobility in Selenium
Proc. Phys. Soc. 76, 826(1960)
11. D. Goldie

The determination of carrier lifetimes and associated mobility magnitudes using photoconductivity recovery dynamics in thin-film amorphous semiconductors
Thin Solid Films 675, 11-15(2019)

12. G. Juška, M. Viliūnas, K. Arlauskas, N. Nekrašas, N. Wyršch, L. Feitknecht
Hole drift mobility in $\mu\text{-Si:H}$
J. Appl. Phys. 89, 4971(2001)
13. G. Juška, K. Arlauskas, N. Nekrašas, J. Stuchlik, X. Niquille, N. Wyršch
Features of charge carrier transport determined from carrier extraction current in $\mu\text{-Si:H}$
J. Non-Cryst. Solids, 299-301, 375-379(2002)
14. G. Juška, K. Genevičius, M. Viliūnas, K. Arlauskas, H. Stuchlíková, A. Fejfar, J. Kočka
New method of drift mobility evaluation in $\mu\text{-Si:H}$, basic idea and comparison with time-of-flight
J. Non-Cryst. Solids, 266-269, 331-335(2000)
15. A. Ashraf, D. M. N. M. Dissanayake, M. D. Eisaman
Measuring charge carrier mobility in photovoltaic devices with micron-scale resolution
Appl. Phys. Lett. 106, 113504(2015)
16. R. A. Street, 1991, Hydrogenated Amorphous Silicon, Cambridge University Press, Cambridge, UK.
17. G. Juška, N. Nekrašas, V. Valentinavičius, P. Meredith, A. Pivrikas
Extraction of photogenerated charge carriers by linearly increasing voltage in the case of Langevin recombination
Phys. Rev. B 84, 155202(2011)
18. B. Tremolet de Villers, C. Tassone, S. Tolbert, B. Schwartz
Improving the Reproducibility of P3HT:PCBM Solar Cells by Controlling the PCBM/Cathode Interface
J. Phys. Chem. Lett. C 113, 18978-18982(2009)
19. S. Venkatesan, E. Ngo, D. Khatiwada, C. Zhang, Q. Quiao
Enhanced Lifetime of Polymer Solar Cells by Surface Passivation of Metal Oxide Buffer Layers
ACS Appl. Mater. Interfaces 7(29), 16093-16100(2015)
20. A. Mozer, N. S. Saricifti
Charge transport and recombination in bulk heterojunction solar cells studied by the photoinduced charge extraction in linearly increasing voltage technique
Appl. Phys. Lett. 86, 112104(2005)
21. S. Fonash, 2010, Solar Cell Device Physics, second ed., Academic Press, Burlington, MA

22. S.M. Mayer
Improved physics in SIMNRA 7
 Nuclear Instruments and Methods in Physics Research B 331, 176-180(2014)
23. G. Juška, K. Arlauskas, M. Viliūnas, J. Kočka
Extraction current transients: New Method of Study of Charge Transport in Microcrystalline Solids
 Phys. Rev. Lett. 84, 4946- (2000)
24. N.F. Mott, E.A. Davis, 1979, Electronic processes in non-crystalline materials, second ed.
 Clarendon, New York
25. M. T. Neukom, N. A. Reinke, B. Ruhstaller
Charge extraction with linearly increasing voltage: A numerical model for parameter extraction
 Solar Energy 85, 1250-1256(2011)
26. G. Hahn, P. Geiger, D. Sontag, P. Fath, E. Bucher
Influence of hydrogen passivation on majority and minority charge carrier mobilities in ribbon silicon
 Solar Energy Materials and Solar Cells 74, 57-63(2002)
27. K. Gmucová, V. Nádaždy, R. Durny
The nature of mobile Hydrogen in a-Si:H- Electrochemical studies
 Solar Energy 80, 694-700(2006)
28. E. Cartier, J. H. Stathis, D. A. Buchanan
Passivation and depassivation of Silicon dangling bonds at the Si/SiO₂ interface by atomic Hydrogen
 Appl. Phys. Lett. 63, 1510(1993)
29. R.A. Street
Recombination in a-Si:H: Defect luminescence
 Phys. Rev. B 21(12), 5775-5784 (1980)
30. N.W. Ashcroft, N.D. Mermin, Solid State Physics, Holt, Rinehart and Winston, 1976
31. W.E. Spear, P.G. LeComber
Substitutional doping of amorphous silicon
 Solid State Communications 17(9), 1193-1196 (1975)
32. M. Green, Third generation photovoltaics: advanced solar energy conversion, Springer, New York, 2003.